Supporting Information

Mechanically Alloyed $NiTiO_3$/Transition Metal Heterostructures: Introducing Oxygen Vacancies for Exceptionally Enhanced Hydrogen Evolution Reaction Activity

Jiaqi Cheng, Pu Liu, Ting Peng, Qinglei Liu, Wenshu Chen, Bowen Liu, Yang Yuan, Wang Zhang, Fang Song, Jiajun Gu, * *and Di Zhang*

Experimental section

Synthesis of $NiTiO_3$:

$NiTiO_3$ nanoparticles were synthesized through a published method.[1] The nickel nitrate (Aladdin, 98.0%) and titanium butoxide (Aladdin, 99.0%) were of analytical grade and were used as received without further purification. These two chemicals, with a molar ratio of 1:1, were dissolved in ethanediol (Aladdin, 98.0%) and stirred for 4 h to form a green clear solution. Then the solution was sealed in an 80 mL Teflon-lined stainless steel autoclave and heated at 180 ℃ for 24 h. The obtained precipitate was washed repeatedly with ethanol and dried overnight in a vacuum oven at 90 ℃. Finally, the precipitate was calcined at 600 ℃ for 2 h in a muffle furnace to obtain the $NiTiO_3$ nanoparticles.

Mechanical alloying:

Starting materials used in mechanical alloying (MA) include TiO_2 (Macklin, anatase, 99.8%), $NiTiO_3$ (home-made), Ni powder (Acros Organics, 99.97%), Co powder (Aladdin, 99.5%), and Fe powder (Aladdin, 99.9%). MA was performed on the planetary ball mill (Nanjing NanDa Instrument Plant, QM-3SP2). The ball milling jar was vacuumed through the suction valve on it *via* a vaccum pump. Then the valve was closed and high-vacuum grease was applied to help to maintain vacuum.

The balls and inner wall of the ball-milling container are usually worn due to the mechanical impactions during MA. Therefore, contamination will be introduced into the materials. We tried to alleviate the contamination by using zirconia balls (diameters: 3 mm and 5 mm, mixed with a mass ratio of 1:1) and zirconia ball milling jars (volume: 50 cm^3, wrapped in stainless steel shell) because the stable zirconia is one of the most wear-resistant options. In addition, zirconia is proved to be inert for hydrogen evolution reaction.[2] The Inductively coupled plasma mass spectrometry (ICP-MS) results of *in situ* $NiTiO_3$/Ni (1:2.7) show that the mass percentage of zirconia is ~2.3% (**Table S4**). The mass ratio of balls to materials was 30:1 (typically 45 g of balls with 1.5 g of active materials). The ball milling jars were vacuumed to prevent TMs powder from oxidation during the MA, and the rotation speed was 400 rad min^{-1}.

Synthesis of *in situ* $NiTiO_3$/Ni: First, Ni powder was ball milled for 40 h. Then TiO_2 was added and ball milled together with Ni powder for another 20 h. Finally, 300 μL of ethanol was included and the ball milling was conducted for another 20 h. The nanosized *in situ* $NiTiO_3$/Ni was obtained.

Synthesis of *ex situ* $NiTiO_3$/TM: First, TM (Fe, Co, or Ni) powder was ball milled for 40 h. Then $NiTiO_3$ was added and ball milled together with Ni powder for another 20 h. Finally, 300 μL of ethanol was included and the ball milling was conducted for another 20 h. The nanosized *ex situ* $NiTiO_3$/TM was obtained.

Synthesis of ball-milled $NiTiO_3$ or ball-milled Ni: $NiTiO_3$ or Ni powder was ball milled for 40 h. Then the ball-milled $NiTiO_3$ or ball-milled Ni was obtained.

Materials characterizations:

XRD results were recorded on an Ultima III X-ray diffractometer (Cu K_α, Rigaku). Raman spectra were acquired with a high spectral resolution confocal Raman microscope (LabRAM HR Evolution, Horiba) using a 532 nm excitation laser. SEM was conducted on a Quanta FEG 250 instrument (FEI). HRTEM, SAED, and element mapping were performed on an ARM-200F TEM (30 kV, JEOL). XPS was carried out on an AXIS Ultra DLD system (Kratos) using Al K_α radiation. All XPS data were calibrated with respect to the C*1s* peak (284.8 eV) of adventitious carbon on the sample surface. EPR experiments were performed at 77 K on an X-band Bruker E580 spectrometer. The specific surface areas of samples were characterized by N_2 adsorption-desorption at 77 K with a Quantachrome Autosorb-IQ device and calculated by BET method. Before measurements, the samples were degassed in vacuum at 150 ℃ for 12 h.

Preparation of working electrodes:

Before tests, the catalysts and carbon black with a mass ratio of 5:1 were evenly mixed in a mortar. Carbon black (Cabot Corporation) was added to improve the electrical conductivity and the dispersibility of the catalysts, as $NiTiO_3$ is a semiconductor with an electrical resistivity of $\sim 1.76\times10^5\ \Omega$ and the obtained ball-milled $NiTiO_3$/TM tend to agglomerate. [3] The obtained mixed powder (10 mg) was prepared into a slurry with the addition of ethanol (250 μL) and Nafion (10 μL), then the slurry was uniformly dispersed *via* sonication with power around 300 W for half an hour. After that, the slurry was dripped on carbon cloth (PHYCHEMI, W0S1009) and dried for electrochemical tests. The loading of the $NiTiO_3$/TM was ~23.2 mg cm^{-2} (corresponding to the optimized performance). Ni and $NiTiO_3$ samples were also prepared following the same procedure. Pt/C (20 *wt.*%, Alfa Aesar) loaded on the carbon cloth with the loading of ~5.0 mg cm^{-2} (corresponding to the optimized performance) was used as a contrast electrocatalyst.

Electrochemical characterizations:

Electrochemical tests were conducted on a Bio-Logic VMP3 work station at room temperature. The HER performance was tested using a three-electrode system in 1 M KOH solution. A graphite rod (99.9995%, Alfa Aesar) and Hg/HgO electrode were used as the counter electrode and reference electrode, respectively. The Hg/HgO electrode was calibrated to reversible hydrogen electrode (RHE) in H_2 saturated 1M KOH solution, establishing relations of E(RHE) = E(Hg/HgO) + 0.925 V. Before the measurements, the electrolyte was bubbled with highly pure N_2 for 30 min. The polarization curves in this work were explored at a scan rate of 2 mV s^{-1} and were *iR*-corrected according to $E_{iR\text{-}corrected} = E_{iR\text{-}free} - iR$, where i is the measured current and R is the solution resistance (2.2 Ω). The electrochemical impedancespectroscopy (EIS) was performed at a potential of −200 mV vs. RHE over frequencies ranging from 100 kHz to 0.1 Hz with a sinusoidal voltage of 10 mV. For simplicity, all cathodic overpotentials, Tafel slopes, and current densities referring to the HER are represented as positive quantities in this manuscript.

C_{dl} calculations:

The C_{dl} can be determined from the cyclic voltammetry curves in a non-reaction potential region (selected as 0.1 to 0.2 V vs. RHE in this work). The C_{dl} values in this work were estimated by:[4]

$$C_{dl} = (j_a - j_c)/(2\cdot v) = (j_a + |j_c|)/(2\cdot v) = \Delta j/(2\cdot v) \qquad \text{(S1)}$$

in which j_a and j_c are the anodic and cathodic voltammetric current density, respectively, recorded at the middle of the select potential range (0.15 V vs. RHE), and v is the scan rate (20, 40, 60, 80, and 100 mV s^{-1}).

DFT calculations:

All calculations were carried out based on density functional theory (DFT) with the Perdew-Burke-Ernzerhof (PBE) form of generalized gradient approximation functional (GGA) by employing the Vienna ab-initio simulation package (VASP).[5–8] A Blöchl's all-electron-like projector augmented wave (PAW) method was used to describe the interactions between valence electrons and ion cores.[9,10] The wave functions at each *k*-point were expanded with a plane wave basis set and a kinetic cutoff energy of 400 eV was applied. Brillouin zone integration was approximated by a sum over specially selected *k*-points using a kjGamma centered Monkhorst–Pack grid, which was set to be 2×2×1.[11] The electron occupancies were determined according to Fermi scheme with an energy smearing of 0.1 eV. Geometries were optimized until the energy was converged to 1.0×10^{-6} eV/atom and the force was converged to 0.01 eV/Å. To describe the van der Waals interactions, a dispersion correction of DFT-D3 was employed. A climbing image nudged elastic band (CINEB) method was used to estimate the energy barriers for the decomposing processes of H_2O molecular on different catalyst surfaces.[12]

The (111) surface of Ni was employed in this work to construct the substrate surface according to TEM results. In order to study the influence of $NiTiO_3$ nanoparticles with and without oxygen vacancies, two small clusters of $NiTiO_3$ with and without oxygen vacancies were loaded on Ni(111) surface, which are denoted as $NiTiO_3$/Ni with O vacancies and $NiTiO_3$/Ni w/o O vacancies, respectively. A model with four layers of 4×2 supercells was chosen for building the pure Ni(111) surface structure, while models with three layers of 4×4 supercells were chosen for building the $NiTiO_3$/Ni-defect and $NiTiO_3$/Ni structures. In the structural optimization calculations, the two bottom layers of atoms were fixed and other atomic layers were allowed to relax for Ni(111) surface, while the most bottom layer of atoms were fixed and all of other atoms were allowed to relax for $NiTiO_3$/Ni-defect and $NiTiO_3$/Ni surfaces. A vacuum layer as large as 15 Å was used along the *c* direction normal to the surface to avoid periodic interactions for all the structures.

According to the method developed by Rossmeisl and Nørskov *et al.*,[13] the free energy change from initial states to final states of the reaction is calculated as follows:

$$\Delta G = \Delta E + \Delta ZEP - T\Delta S \tag{S2}$$

where ΔE is the total energy change obtained from DFT calculations, ΔZPE is the zero point energy (ZPE) corrections, which were obtained using the harmonic vibrational frequency calculations. T is room temperature (298.15 K), and the ΔS is the change in entropy. ΔZPE and $T\Delta S$ values of adsorbed species were obtained *via* the frequency calculation by:[14,15]

$$ZPE = \frac{1}{2}\sum \mathrm{h}v_i \tag{S3}$$

$$TS_v = k_B T\left[\sum\nolimits_K \ln\left(\frac{1}{1-e^{-hv/\mathrm{k}_B T}}\right) + \sum\nolimits_K \frac{hv}{k_B T}\frac{1}{(e^{hv/\mathrm{k}_B T}-1)}\right] \tag{S4}$$

where k_B is the Boltzmann constant, v is vibrational frequency for the intermediates, which are obtained from DFT calculations using VASP.

Table S1. The input mass ratios of TiO_2 to Ni and the output mole ratios of *in situ* $NiTiO_3$ to Ni.

	Ratio 1	Ratio 2	Ratio 3	Ratio 4	Ratio 5	Ratio 6
Mass ratios of TiO_2 to Ni	1:10	2:10	3:10	5:10	7:10	9:10
Mole ratios of $NiTiO_3$ to Ni	1:13.6	1:6.8	1:4.5	1:2.7	1:1.9	1:1.5

We prepared a series of *in situ* $NiTiO_3$/Ni samples with various compositions *via* regulating the input mass ratios of TiO_2 to Ni. As the $NiTiO_3$ in *in situ* $NiTiO_3$/Ni was full of oxygen vacancies and the mass ratios could deviate from the stoichiometry, mole ratios were used to evaluate the ratios of $NiTiO_3$ to Ni in *in situ* $NiTiO_3$/Ni. The equation is as below.

$$\text{mole ratio of } \textit{in situ} \text{ NiTiO}_3 \text{ to Ni} = \frac{\text{input mass}\left(\text{TiO}_2\right) \times 58.7}{\text{input mass (Ni)} \times 79.9 - \text{input mass}\left(\text{TiO}_2\right) \times 58.7} \qquad \text{(S5)}$$

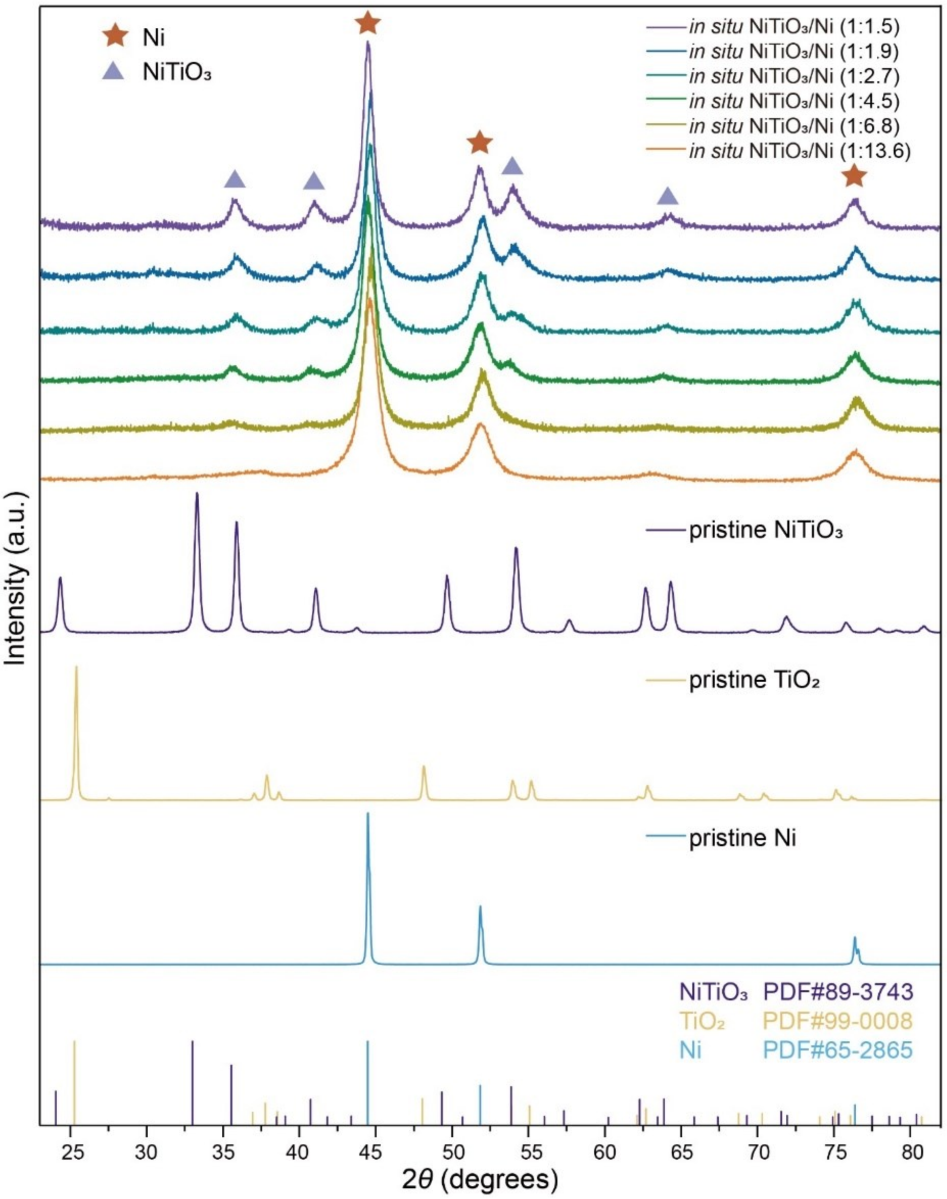

Figure S1. XRD results of *in situ* $NiTiO_3$/Ni with different mole ratios. Results of the pristine $NiTiO_3$, TiO_2, and Ni are also listed for comparison.

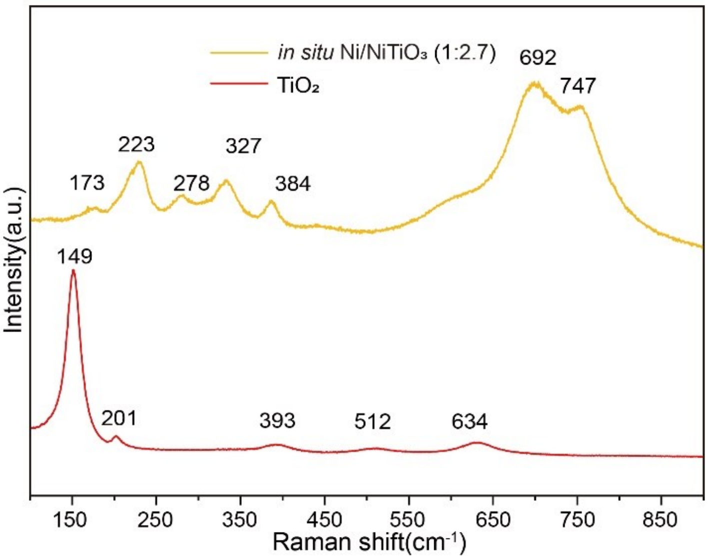

Figure S2. Raman spectra of *in situ* $NiTiO_3/Ni$ (1:2.7) and TiO_2. After MA the Raman signal of TiO_2 disappears, indicating that TiO_2 is depleted.

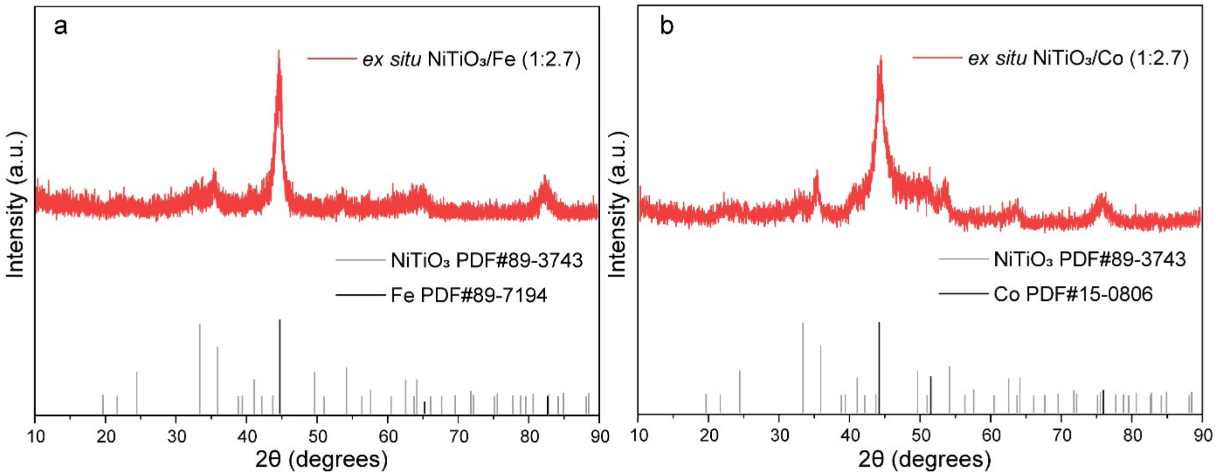

Figure S3. XRD results of a) *ex situ* $NiTiO_3/Fe$ (1:2.7) and b) *ex situ* $NiTiO_3/Co$ (1:2.7) obtained *via* MA.

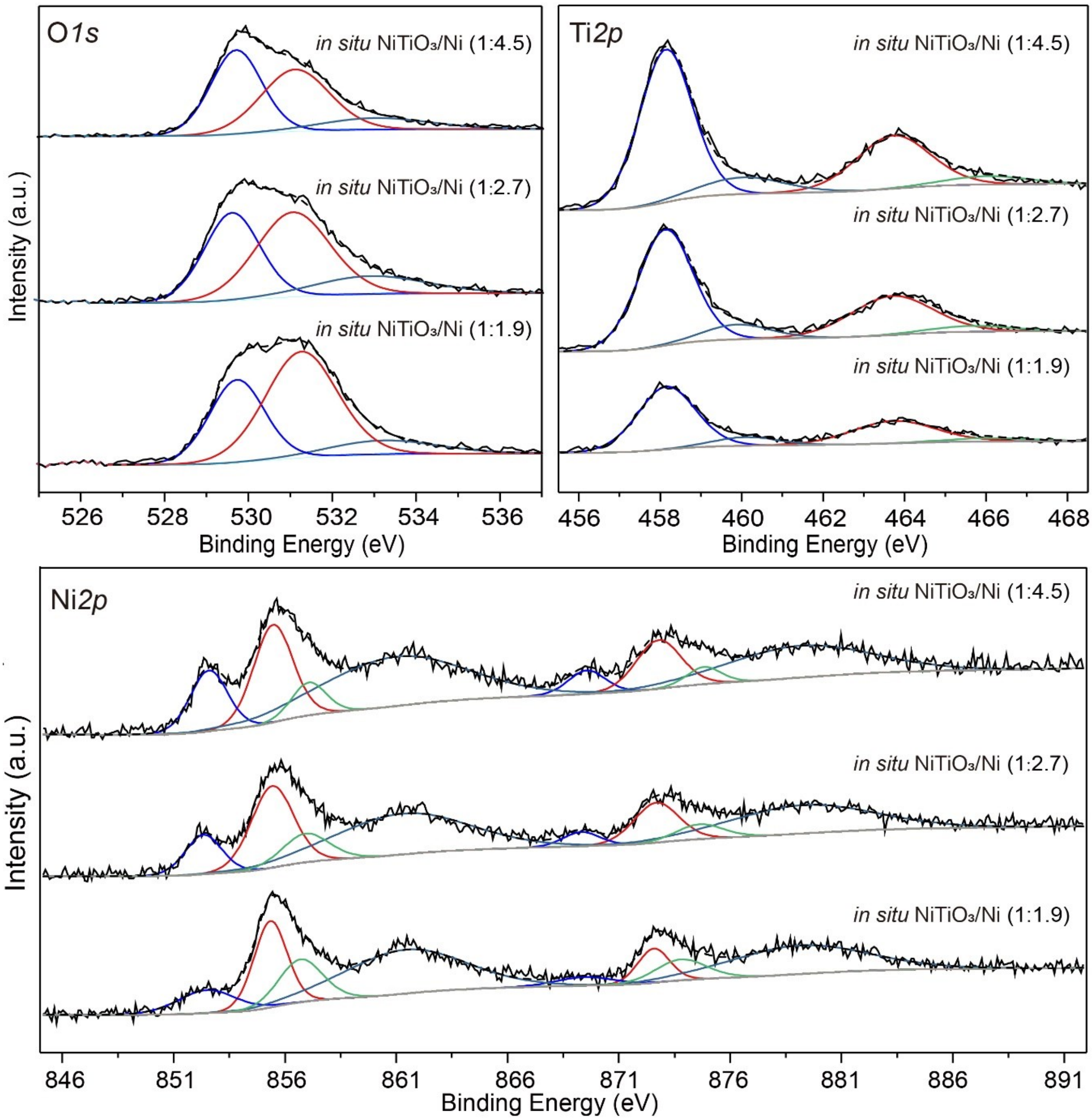

Figure S4. XP spectra of O*1s*, Ti*2p*, and Ni*2p* of *in situ* $NiTiO_3$/Ni (1:1.9), *in situ* $NiTiO_3$/Ni (1:2.7), and *in situ* $NiTiO_3$/Ni (1:4.5), respectively.

Table S2. Surface oxygen vacancies concentration of *in situ* $NiTiO_3/Ni$, pristine and ball-milled $NiTiO_3$ calculated from the XPS results.

Sample	O*1s*			mole ratio of Ti:O_L	concentration of oxygen vacancies (O_V)
	O_L	O_{OH}	O_S		
pristine $NiTiO_3$	83.1%	15.4%	1.5%	2.051	18.9%
ball-milled $NiTiO_3$	47.7%	49.0%	3.3%	2.245	25.2%
in situ $NiTiO_3/Ni$ (1:2.7)	35.5%	50.8%	13.7%	2.432	31.6%

The concentration of surface oxygen vacancies (O_V) was calculated by:[16,17]

O_V (%) = (the mole ratio of Ti)×3 － (the mole ratio of O_L). (S6)

It should be noted that the concentration of surface oxygen vacancies is commonly higher than that of the bulk material. The concentration of oxygen vacancies on the surface of pristine $NiTiO_3$ is 18.9% and the *in situ* $NiTiO_3/Ni$ is 31.6%.

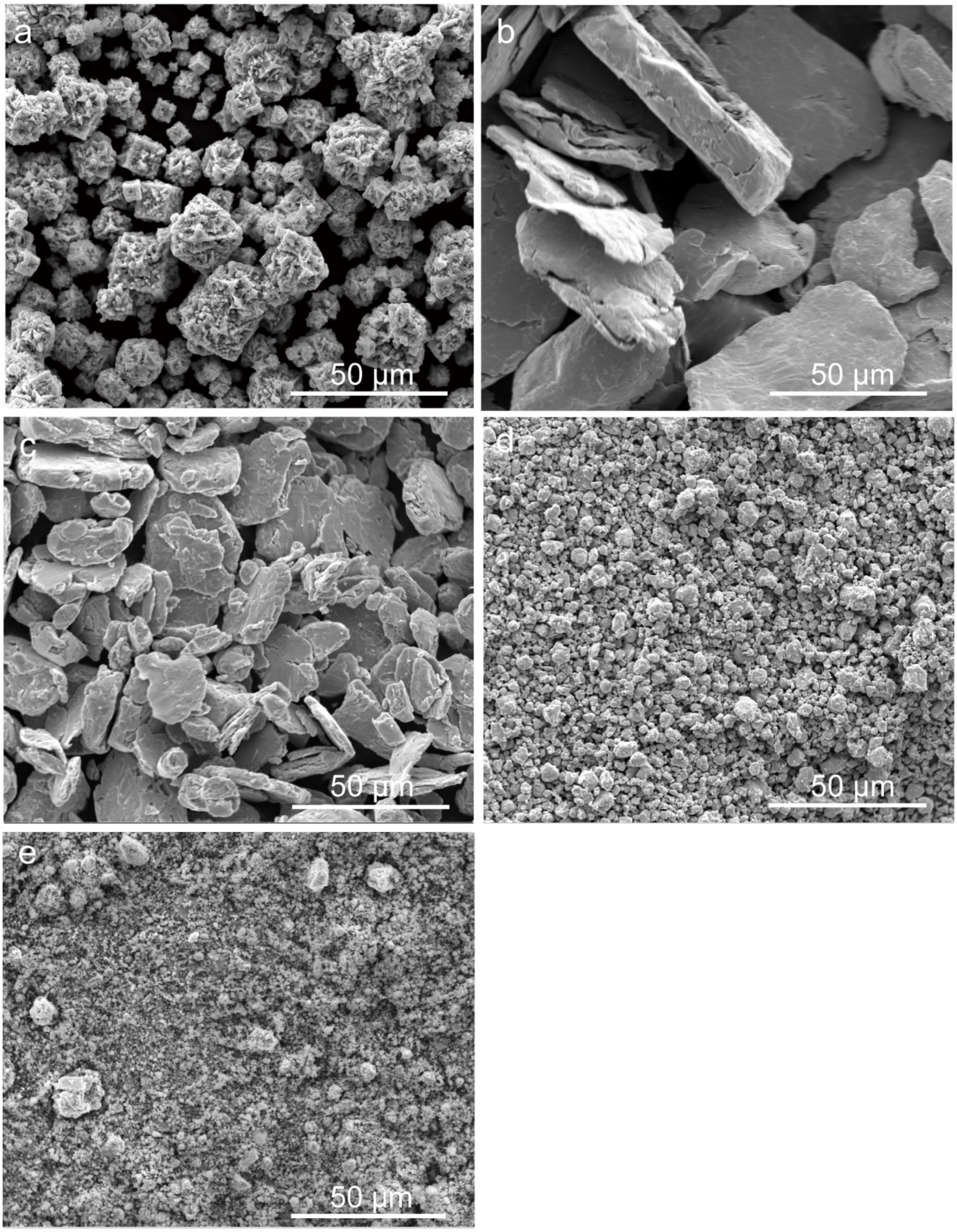

Figure S5. a) SEM image of the pristine nickel powder purchased from Acros Organics. b) and c) SEM images of the nickel powder after ball milling for 20 and 40 hours, respectively. d) SEM image of the powder after adding TiO_2 into c) and ball milling for another 20 hours. e) SEM image of the powder after adding ethanol into d) and ball milling for 20 hours.

During MA, the Ni powder was first flattened and connected *via* continuous mechanical impaction, accompanying with increased particle sizes. Then, the particle sizes of Ni gradually decreased with further milling and the particle morphology appeared to be spherical owing to work-hardening and fatigue failure phenomena.[18,19] With the addition of TiO_2 powder, the Ni reacted with TiO_2. Meanwhile, the brittle and hard TiO_2 particles also acted as grinding aids to further fragilize the nickel particles. Finally, the process control agent (ethanol) was added to prevent particle aggregation and increase the grinding efficiency, which accelerated the grain fragilization and nanophase generation /falling-off during the MA. The nanosized *in situ* $NiTiO_3$/Ni was obtained.

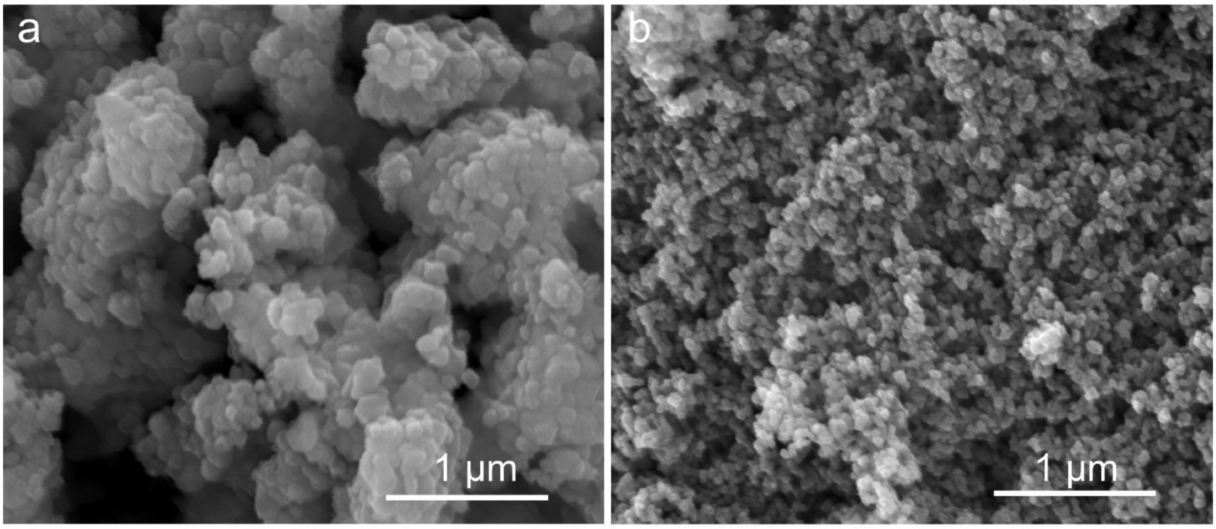

Figure S6. SEM images of a) the pristine TiO_2 powder purchased from Macklin and b) the home-made $NiTiO_3$ powder.

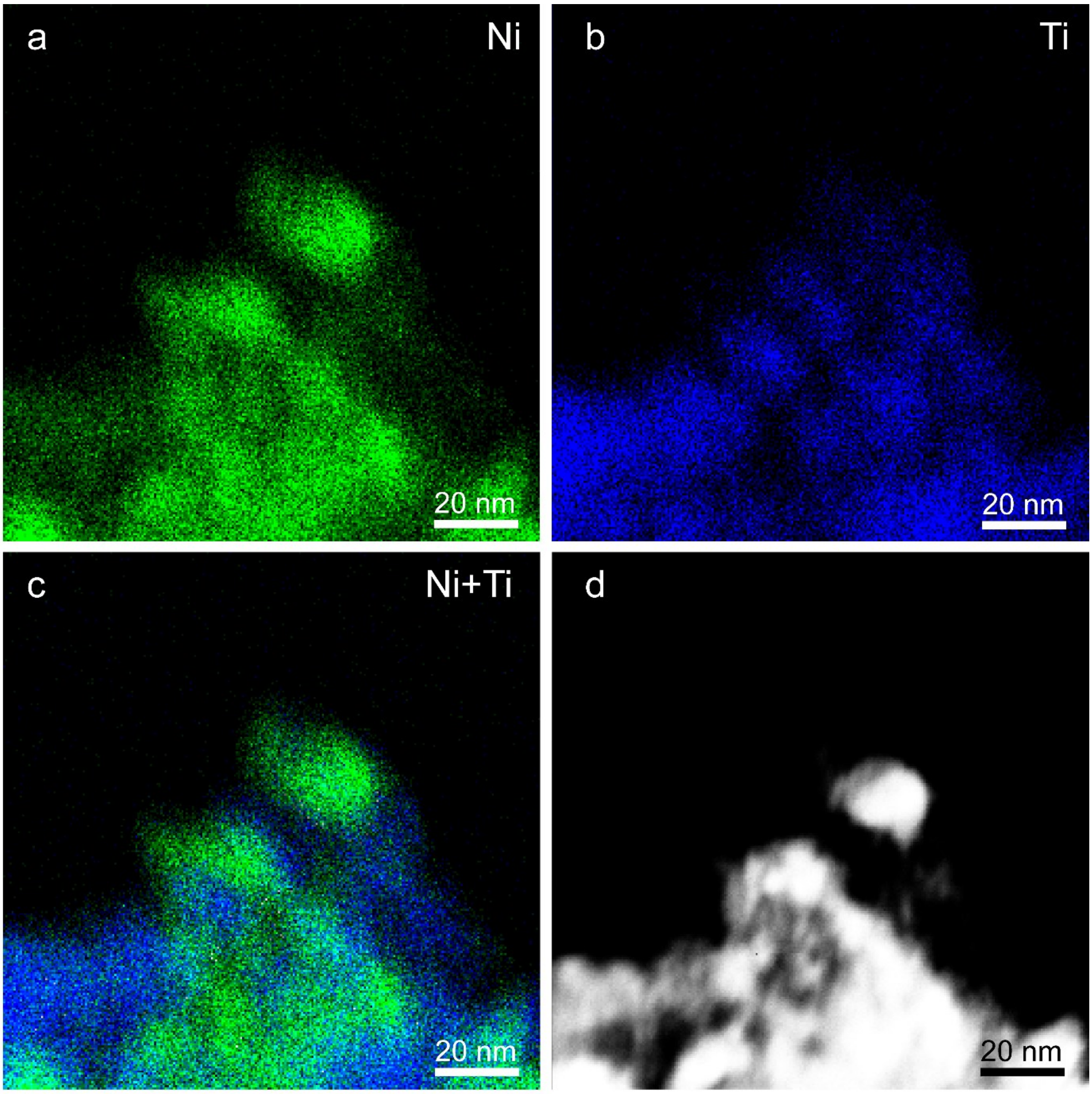

Figure S7. a-c) EDS mappings of the *in situ* $NiTiO_3$/Ni (1:2.7). d) Bright-field (BF) TEM image of the *in situ* $NiTiO_3$/Ni (1:2.7).

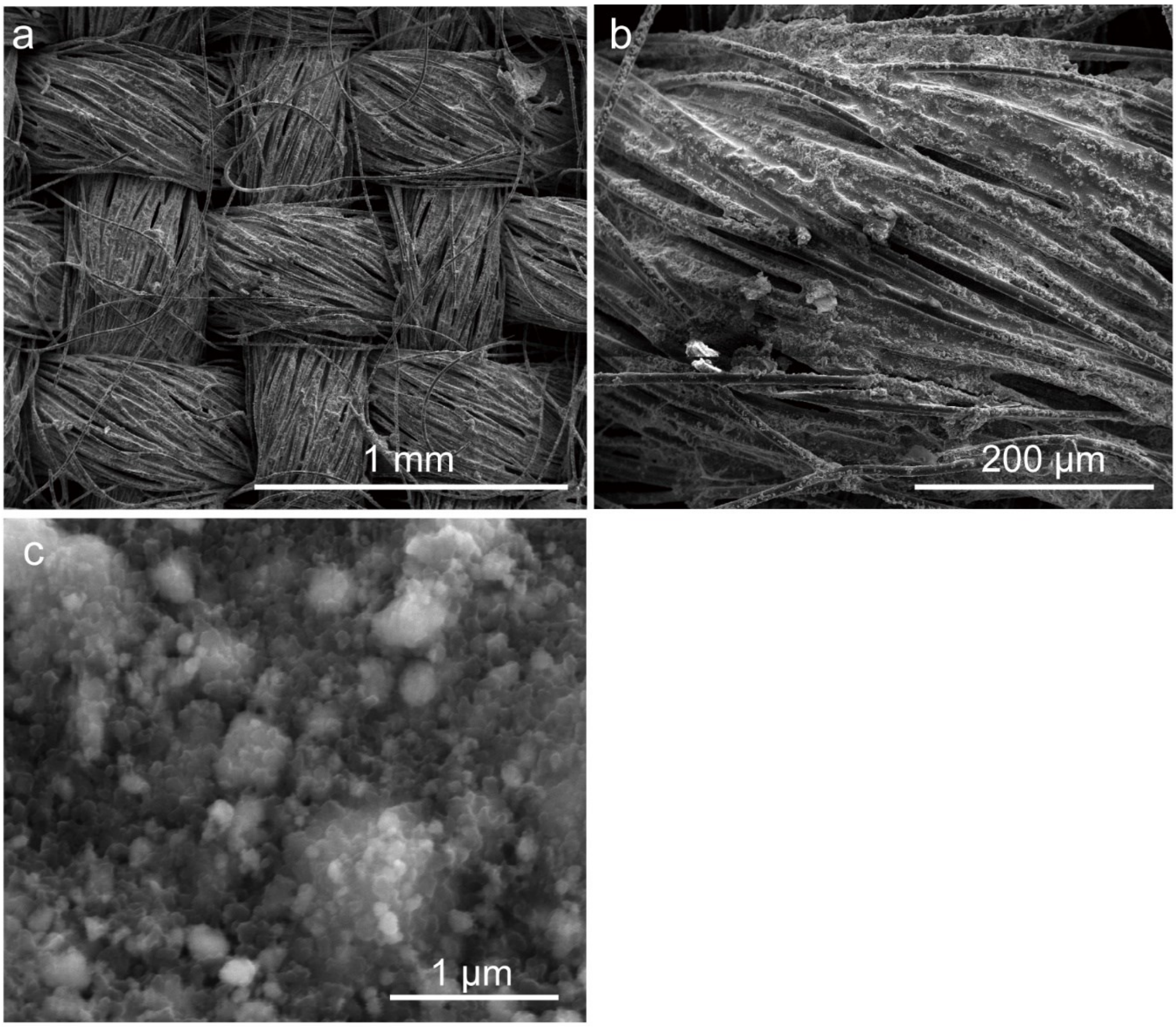

Figure S8. SEM images of *in situ* $NiTiO_3$/Ni loaded on the carbon cloth.

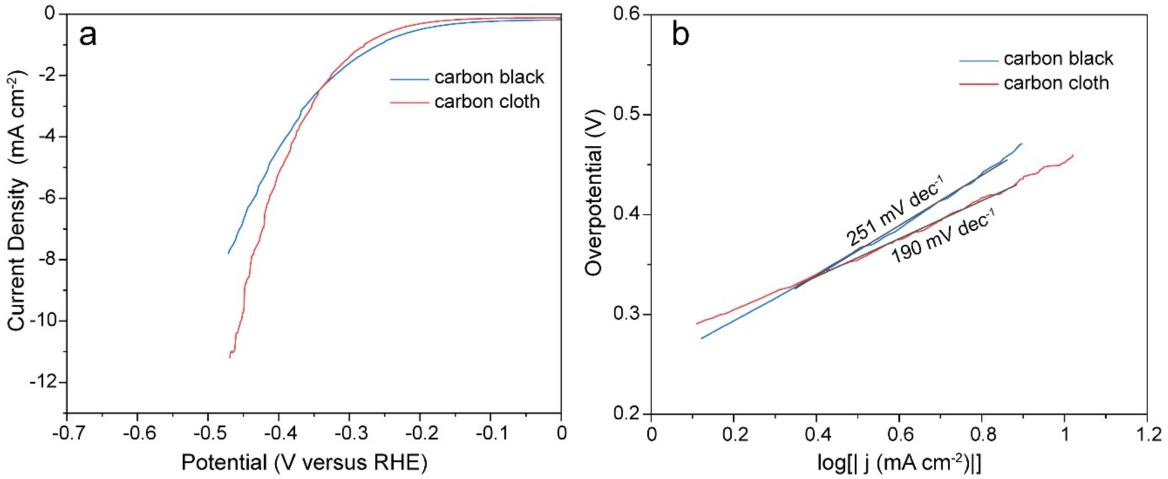

Figure S9. a) Polarization curves and b) Tafel plots of carbon cloth and carbon black.

As exhibited in **Figure S9**, the carbon cloth and carbon black exhibit poor HER performance with overpotential of ~393 mV and ~413 mV at the current density of 5 mA cm^{-2}, and with Tafel slope of ~190 mV dec^{-1} and ~251 mV dec^{-1}, respectively. Therefore, we believe that they can hardly contribute to the high HER performance of catalysts in this work.

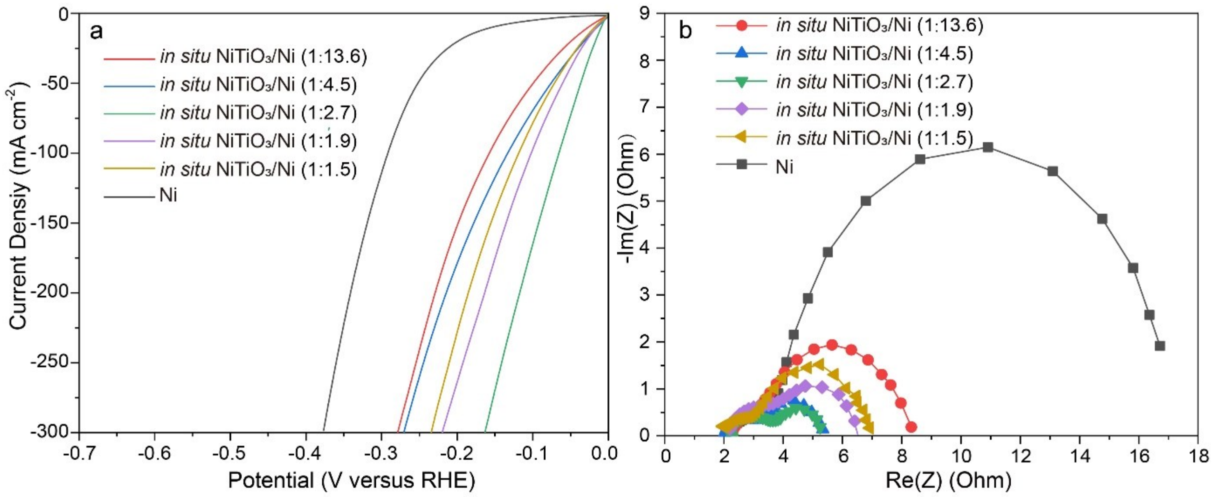

Figure S10. a) LSV curves and b) EIS Nyquist plots of *in situ* $NiTiO_3$/Ni with different mole ratios.

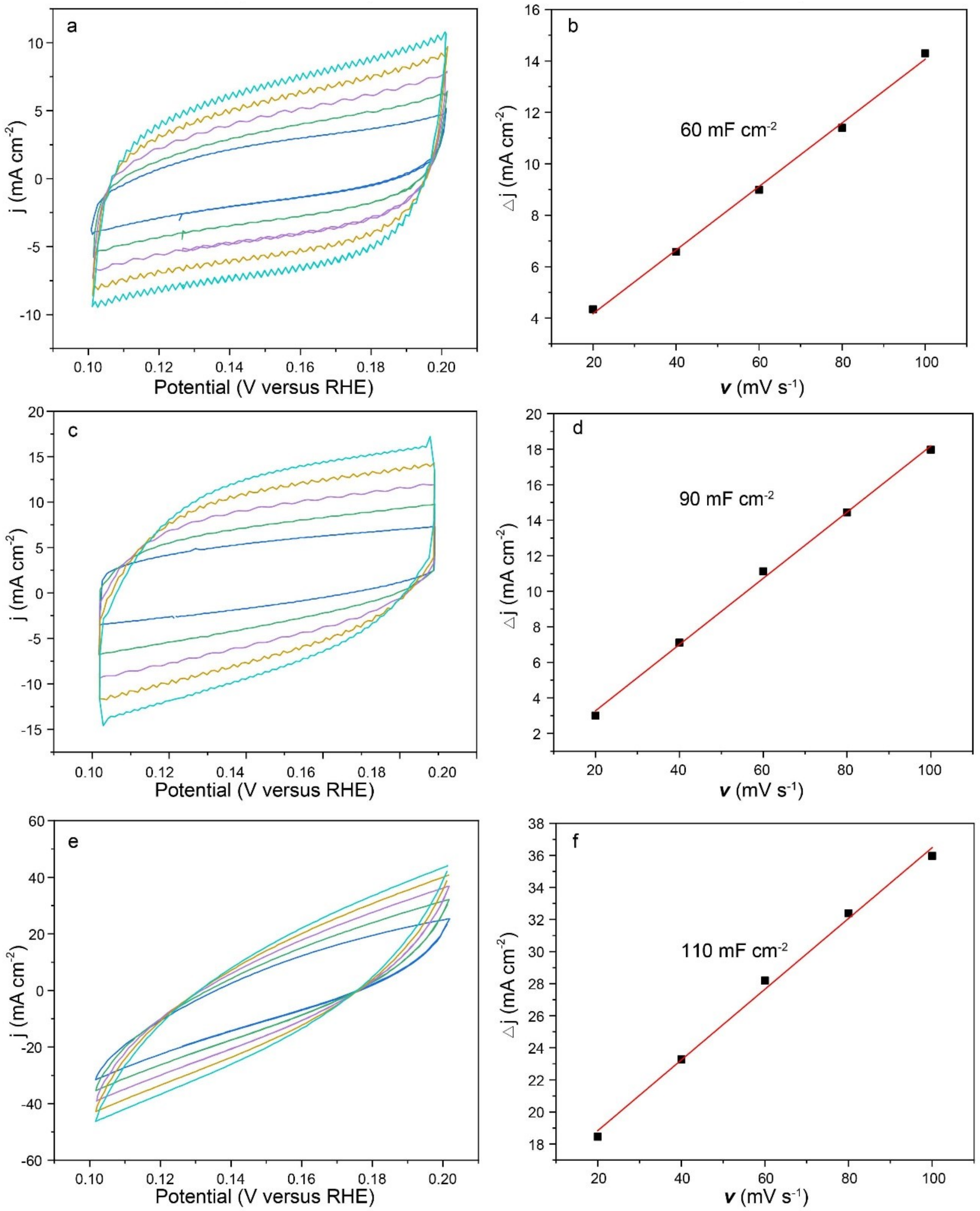

Figure S11. C$_{dl}$ characterizations of a) and b) the pristine Ni, c) and d) Pt/C, e) and f) *in situ* NiTiO$_3$/Ni (1:2.7).

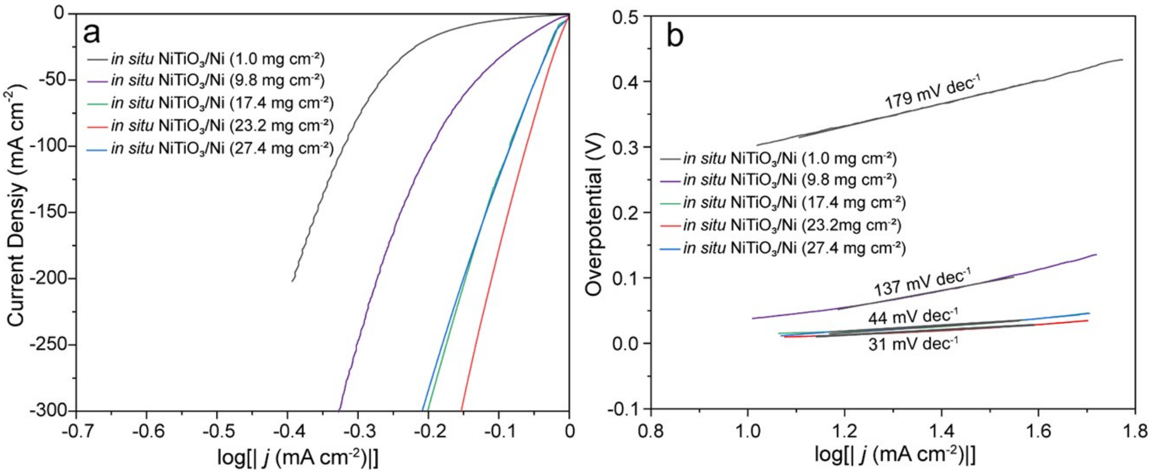

Figure S12. a) LSV curves and b) Tafel plots of *in situ* $NiTiO_3$/Ni with various mass loading. The mole ratio of *in situ* $NiTiO_3$/Ni is 1:2.7.

The HER performance of *in situ* $NiTiO_3$/Ni with various mass loading is exhibited in **Figure S12**. With the mass loading rising from 1.0 mg cm^{-2} to 23.2 mg cm^{-2}, the larger surface area of carbon cloth is covered, leading to increased HER performance (η_{10}: from ~153 mV to ~10 mV, Tafel slop: from ~158 mV dec^{-1} to ~31 mV dec^{-1}). However, with the mass loading further rising, the catalyst is overloaded and the electron transport may be affected, resulting in decreased catalytic performance.

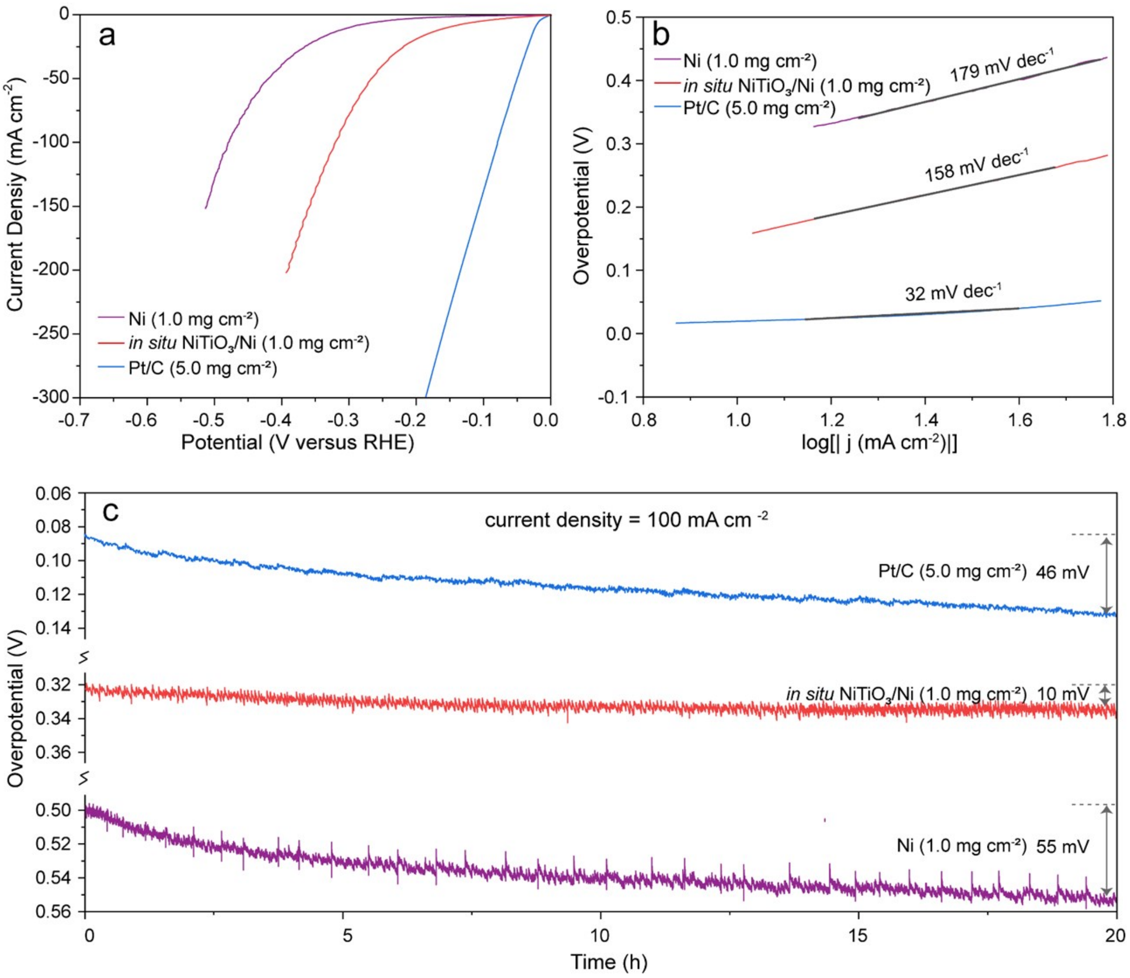

Figure S13. a) LSV curves b) Tafel plots and c) Long-term stability of the *in situ* $NiTiO_3$/Ni (1.0 mg cm^{-2}), Pt/C (5.0 mg cm^{-2}) and Ni (1.0 mg cm^{-2}). The long-term stability tests were employed at current density of 100 mA cm^{-2}. The mole ratio of *in situ* $NiTiO_3$/Ni is 1:2.7.

The results in **Figure S13** show that η_{10} of *in situ* $NiTiO_3/Ni$ (1.0 mg cm^{-2}), Ni (1.0 mg cm^{-2}), and Pt/C (5.0 mg cm^{-2}) is ~153 mV, ~300 mV, and ~21 mV, respectively. The Tafel slope of them is ~158 mV dec^{-1}, ~179 mV dec^{-1}, and ~32 mV dec^{-1}, respectively. Therefore, under such loading conditions, the HER catalytic activity of *in situ* $NiTiO_3/Ni$ (1.0 mg cm^{-2}) is far inferior to Pt/C (5.0 mg cm^{-2}). In terms of stability, after working for 20 hours at the density of 100 mA cm^{-2}, *in situ* $NiTiO_3/Ni$ (1.0 mg cm^{-2}) only degrades ~10 mV in performance, while Ni (1.0 mg cm^{-2}) and Pt/C (5.0 mg cm^{-2}) degrades ~55 mV and ~46 mV, respectively. Therefore, the stability of *in situ* $NiTiO_3/Ni$ is still better than Pt/C and Ni.

The performance gap between *in situ* $NiTiO_3/Ni$ (1.0 mg cm^{-2}) and Pt/C (5.0 mg cm^{-2}) is mainly due to the greatly decreased catalytic area. The *in situ* $NiTiO_3/Ni$ particles agglomerated severely as a result of mechanical compaction during MA. Although ultrasonic was used to disperse particles during the preparation of catalytic slurry, the effect is limited. When the loading is only 1.0 mg cm^{-2}, the particles can only cover small surface area of carbon cloth (see SEM images in **Figure S14a** and **b**). As a comparison, Pt/C is of very good dispersibility. With the loading of 5.0 mg cm^{-2}, Pt/C can completely cover the surface of carbon cloth to obtain the maximum catalytic activity area (**Figure S14c** and **d**). Besides that, the electrochemical active surface area results in **Figure S15** reveal that the C_{dl} of Pt/C (5.0 mg cm^{-2}) is ~21 times of *in situ* $NiTiO_3/Ni$ (1.0 mg cm^{-2}), which also support that the effective catalytic area of *in situ* $NiTiO_3/Ni$ (1.0 mg cm^{-2}) is insufficient.

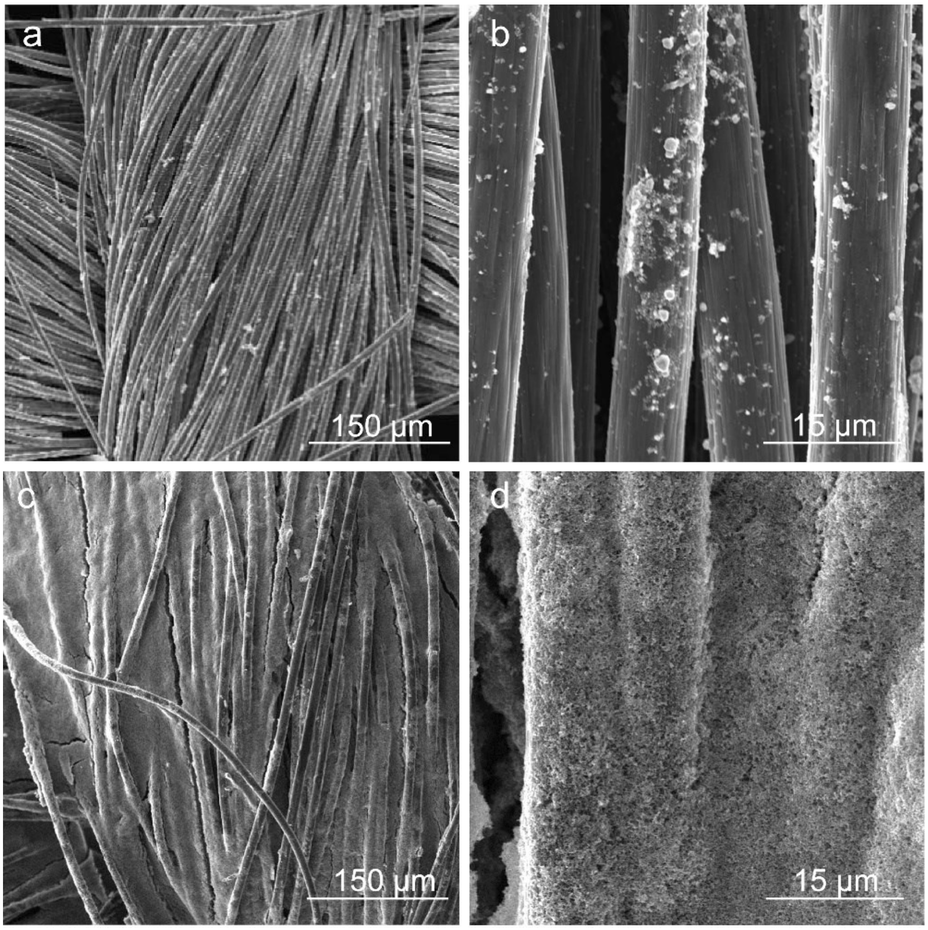

Figure S14. SEM images of a) *in situ* $NiTiO_3/Ni$ (1.0 mg cm^{-2}) and b) Pt/C (5.0 mg cm^{-2}) loaded on carbon cloth. The mole ratio of *in situ* $NiTiO_3/Ni$ is 1:2.7.

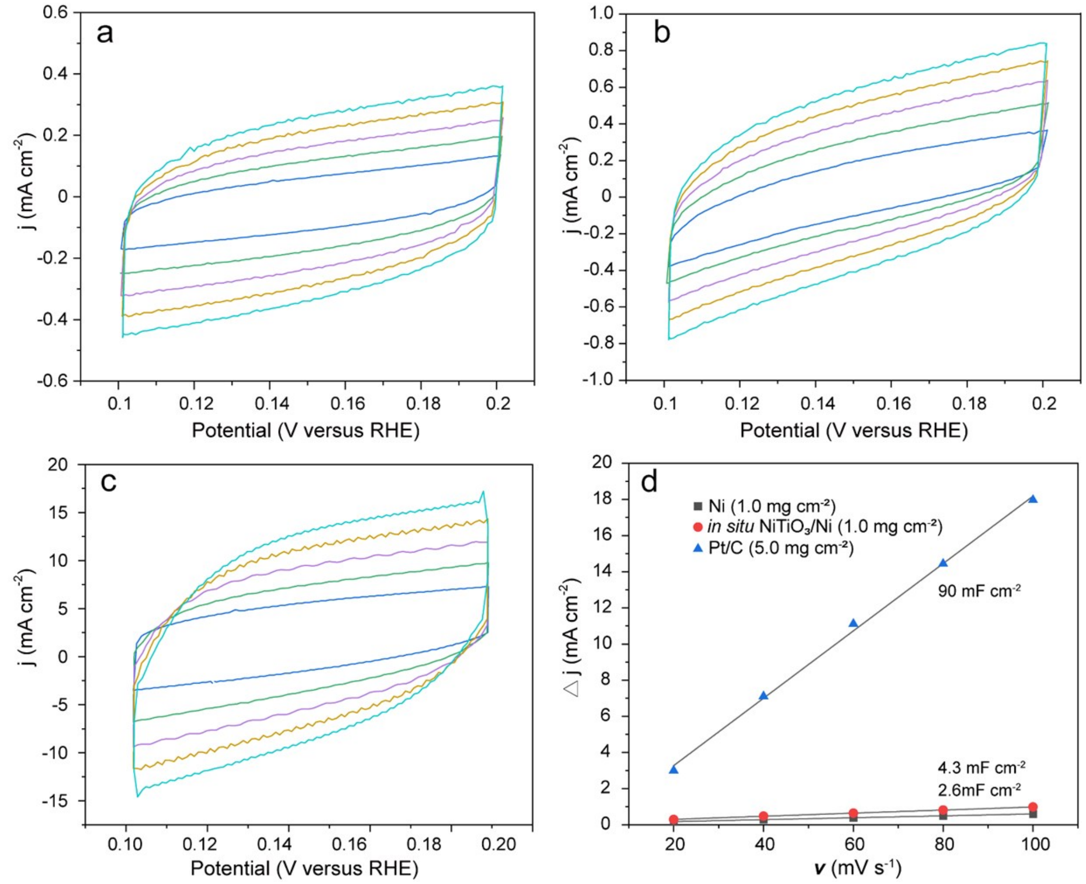

Figure S15. CV curves of a) Ni (1.0 mg cm^{-2}) b) *in situ* NiTiO$_3$/Ni (1.0 mg cm^{-2}) and c) Pt/C (5.0 mg cm^{-2}). d) C_{dl} results of Ni (1.0 mg cm^{-2}), *in situ* NiTiO$_3$/Ni (1.0 mg cm^{-2}) and Pt/C (5.0 mg cm^{-2}). The mole ratio of *in situ* NiTiO$_3$/Ni is 1:2.7.

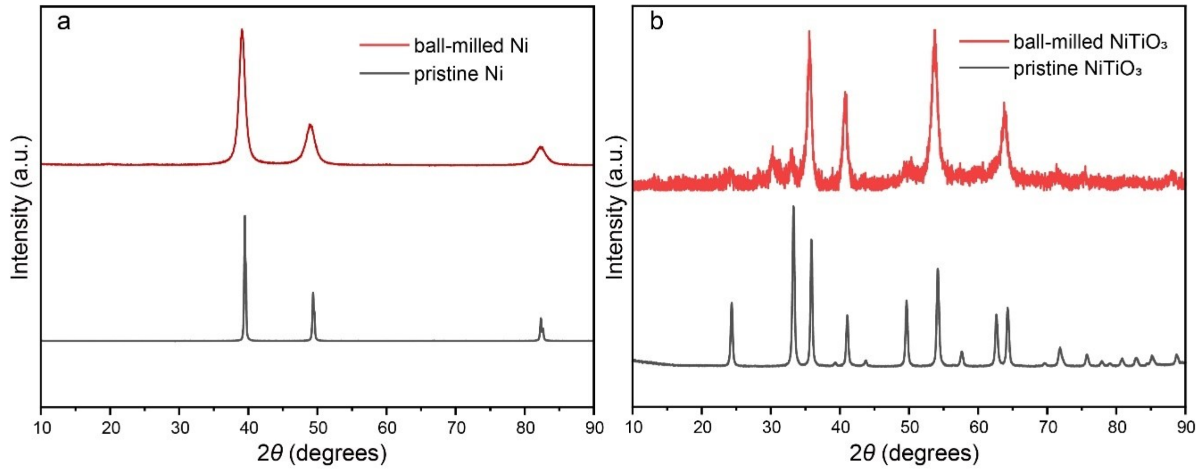

Figure S16. XRD results of a) nickel powder and b) synthesized $NiTiO_3$ before and after ball milling.

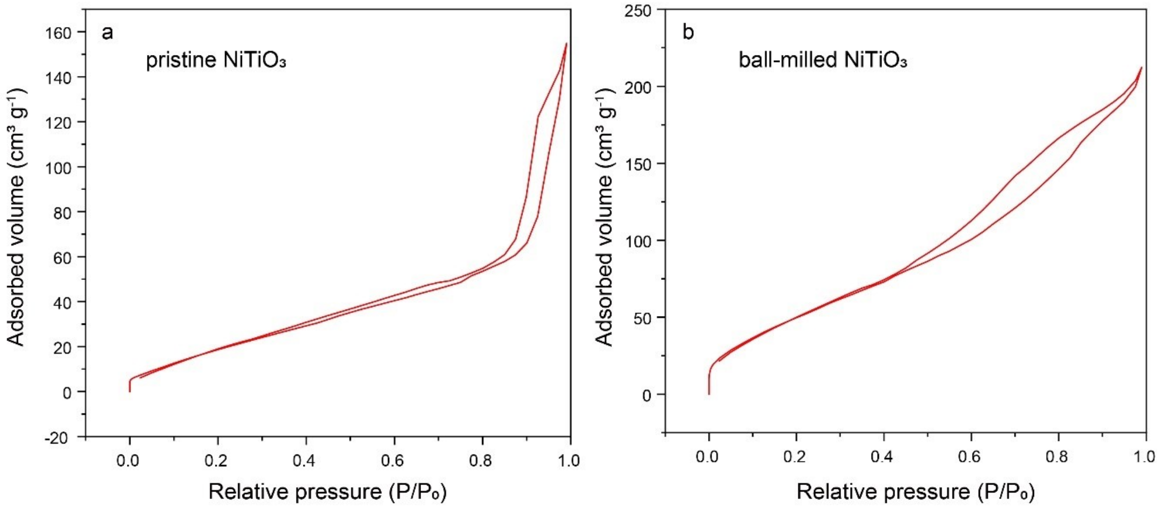

Figure S17. N_2 sorption isotherm curves of a) the pristine $NiTiO_3$ and b) ball-milled $NiTiO_3$.

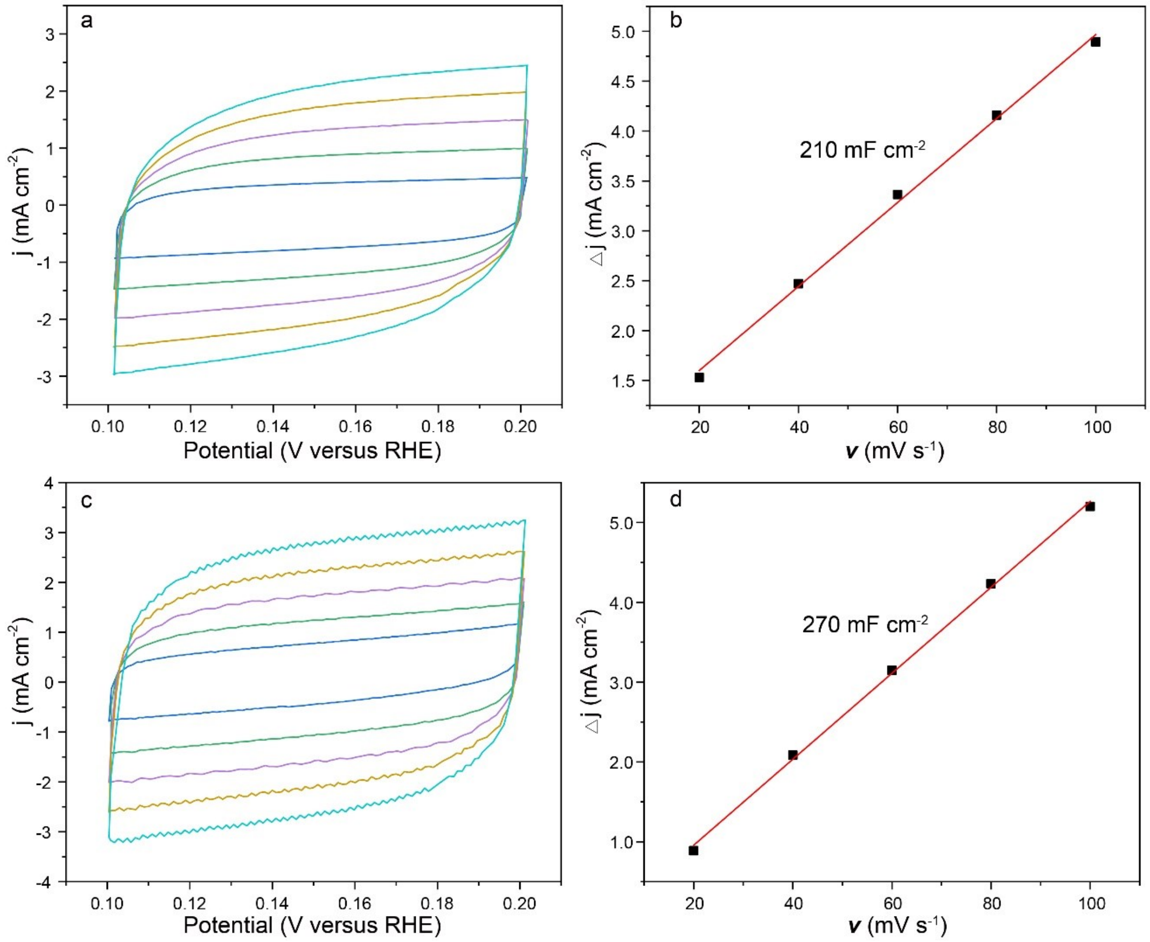

Figure S18. C_{dl} characterizations of a) and b) the pristine $NiTiO_3$, c) and d) ball-milled $NiTiO_3$.

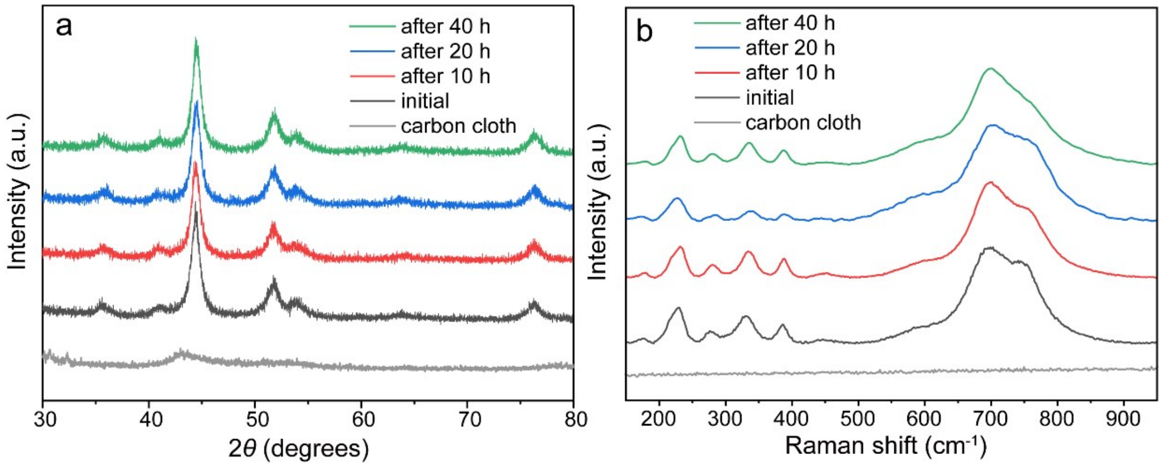

Figure S19. a) XRD results and b) Raman results of *in situ* $NiTiO_3/Ni$ before HER and after HER for 10 hours, 20 hours, and 40 hours at current density of 100 mA cm^{-2}. These catalysts are loaded on carbon cloth, so the characterization of carbon cloth as the blank sample is also listed.

The *in situ* $NiTiO_3/Ni$ was loaded on carbon cloth and worked at current density of 100 mA cm^{-2} for 10 hours, 20 hours, and 40 hours, respectively. Then XRD and Raman were employed. The XRD (**Figure S19a**) and Raman (**Figure 19b)** results reveal that even after 40 hours' reaction the post reaction sample shows no obvious change in chemical composition. Therefore, we believe that *in situ* $NiTiO_3/Ni$ is stable under this strong reducing atmosphere.

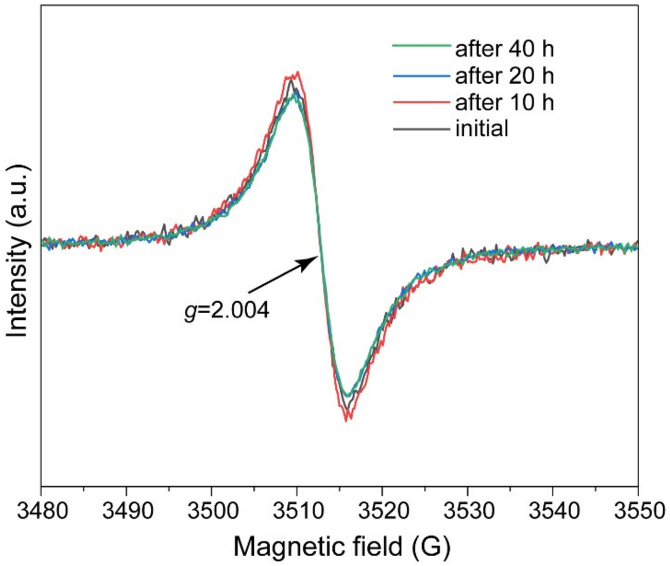

Figure S20. a) EPR results of *in situ* $NiTiO_3/Ni$ before reaction and after reaction at a current density of 100 mA cm^{-2} for 10 hours, 20 hours, and 40 hours, respectively. The peak position of the EPR results here is slightly different from the results in the manuscript, and the *g* factor remains the same. This is due to the little difference in the parameter of attenuator, which does not influent the result analysis.

we tracked the oxygen vacancy concentration of *in situ* $NiTiO_3/Ni$ according to the reaction time *via* the EPR. The results in **Figure S20** show that the oxygen vacancy concentration increases to ~103% of the initial state after 10 hours, and decreases to ~90% after 20 hours, then remains ~90% after 40 hours. The reason for the slight increase of oxygen vacancy concentration is unsureat present, but we presume that this phenomenon may due to the activation of catalyst [20] at the early edge of HER. The decrease may be related to the poisoning of some active sites of $NiTiO_3$. Overall, the oxygen vacancy concentration can remain ~90%, indicating that oxygen vacancies are basically stable during HER.

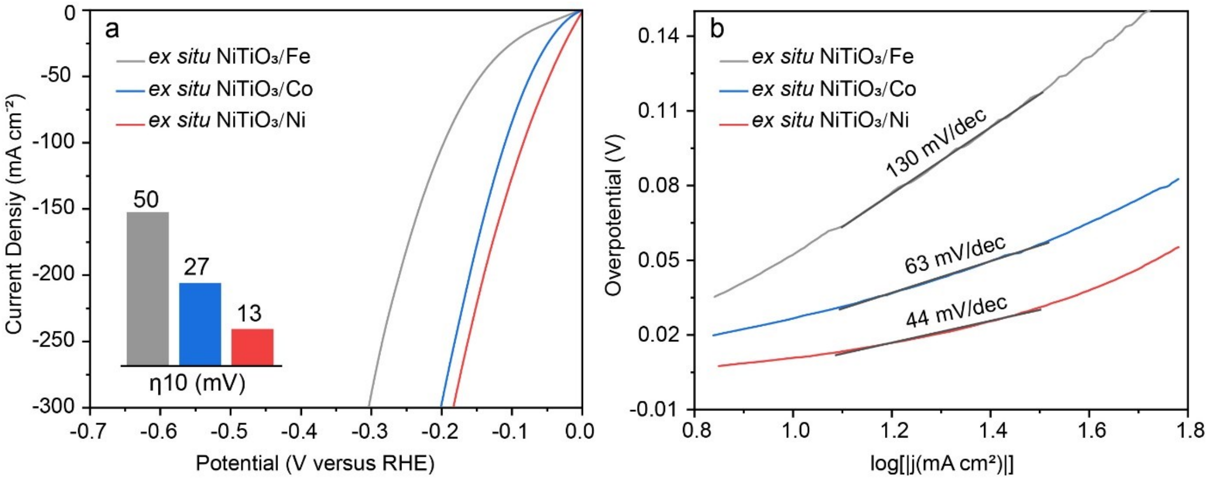

Figure S21. a) Polarization curves and b) Tafel plots of *ex situ* $NiTiO_3$/Ni (1:2.7), $NiTiO_3$/Co (1:2.7), and $NiTiO_3$/Fe (1:2.7), respectively.

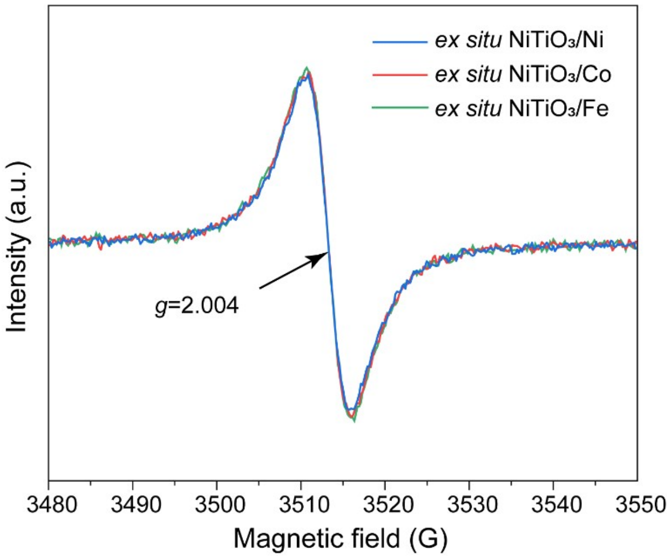

Figure S22. EPR results of *ex situ* $NiTiO_3$/Ni, *ex situ* $NiTiO_3$/Co, and *ex situ* $NiTiO_3$/Fe.

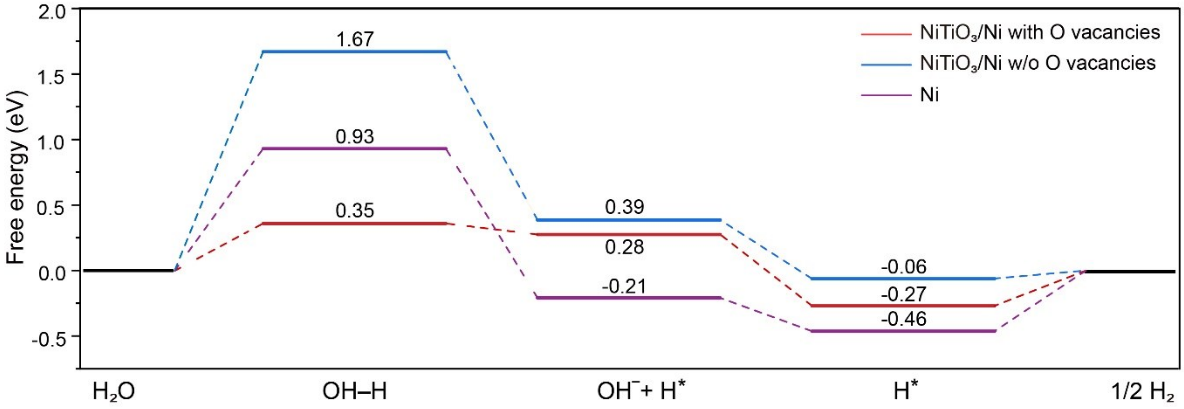

Figure S23. Calculated free energy diagram of Volmer step and Tafel step of Ni, $NiTiO_3$/Ni without oxygen vacancies, and $NiTiO_3$/Ni with oxygen vacancies, respectively.

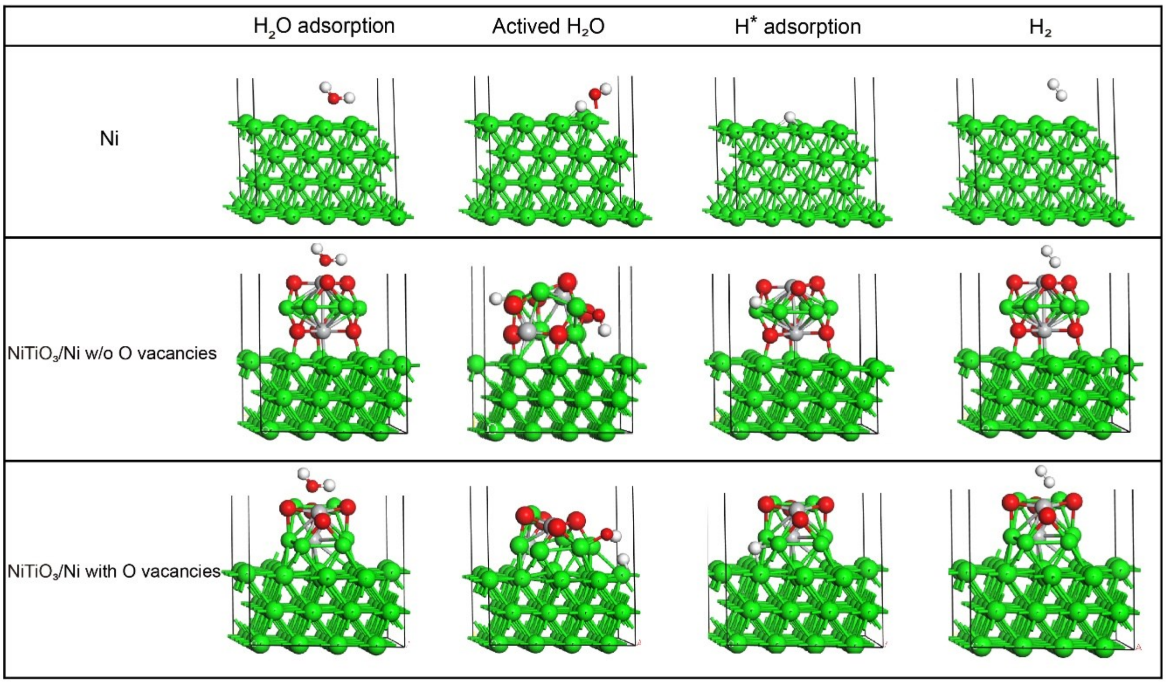

Figure S24. The crystal models of Ni, $NiTiO_3$/Ni without oxygen vacancies, and $NiTiO_3$/Ni with oxygen vacancies during the hydrogen evolution process. Green balls: Ni; Grey balls: Ti; Red balls: O; white balls: H.

Table S3. Comparison of the HER performance of $NiTiO_3$/TM with that of the state-of-the-art materials in 1 M KOH solution.

Catalysts	η_{10} (mV)	Tafel Slopes (mV dec^{-1})	Solution	Types	Ref.
in situ $NiTiO_3$/Ni (1:2.7)	10	31	1 M KOH	Non-precious metal catalyst	this work
Ru-NC	12	14	1 M KOH	Precious metal-containing catalysts	21
ex situ $NiTiO_3$/Ni (1:2.7)	13	44	1 M KOH	Non-precious metal catalyst	this work
Pt-Ni/Ni_4N	13	29	1 M KOH	Precious metal-containing catalysts	22
FeP/Ni_2P	14	24	1 M KOH	Non-precious metal catalyst	23
$MoNi_4$	15	30	1 M KOH	Non-precious metal catalyst	24
$Cu_{53}Ru_{47}$	15	30	1 M KOH	Precious metal-containing catalysts	25
ex situ $NiTiO_3$/Co (1:2.7)	27	63	1 M KOH	Non-precious metal catalyst	this work
Pt-Ni ASs	28	27	1 M KOH	Precious metal-containing catalysts	26
Ru–MoO_2	29	31	1 M KOH	Precious metal-containing catalysts	27
$NiCo_2S_4$ NWs	41	37	1 M KOH	Non-precious metal catalyst	28
C-MoS_2	45	46	1 M KOH	Non-precious metal catalyst	29
Mo_2C@2D-NPC	45	46	1 M KOH	Non-precious metal catalyst	30
Ru-Ru_2P@NPC	46	40	1 M KOH	Precious metal-containing catalysts	31
N,P-doped Mo_2C@C Nanospheres	47	71	1 M KOH	Non-precious metal catalyst	32
Ni_5P_4 (pellet)	49	98	1 M KOH	Non-precious metal catalyst	33
ex situ $NiTiO_3$/Fe	50	130	1 M KOH	Non-precious metal catalyst	this work
$NiCo_2P_x$ nanowires	58	34.3	1 M KOH	Non-precious metal catalyst	34
Nanoporous Co_2P	60	40	1 M KOH	Non-precious metal catalyst	35
MoP_2NS/CC	67	70	1 M KOH	Non-precious metal catalyst	36
Mo_2C@NPC	72	52	1 M KOH	Non-precious metal catalyst	30
Ni-FeP/TiN/CC	75	73	1 M KOH	Non-precious metal catalyst	37
Co_3S_4/EC-MOF	84	83	1 M KOH	Non-precious metal catalyst	38
$Ni_{1-x}Co_xSe_2$ nanosheet	85	52	1 M KOH	Non-precious metal catalyst	39
Co_1/PCN	89	52	1 M KOH	Non-precious metal catalyst	40
Mo_2C/NCF	100	65	1 M KOH	Non-precious metal catalyst	41
Ni/$NiTiO_3$ (Chemical method)	196	118	1 M KOH	Non-precious metal catalyst	42

Table S4. Inductively coupled plasma mass spectrometry (ICP-MS) results of *in situ* $NiTiO_3$/Ni (1:2.7). The results show that the mass percentage of zirconia in *in situ* $NiTiO_3$/Ni (1:2.7) is ~2.3%.

	Ni (%)	Ti (%)	Zr (%)
#1	61.50	17.79	2.329
#2	61.40	18.00	2.333
#3	61.37	17.96	2.320
#4	61.14	17.98	2.310
#5	60.88	17.73	2.284
Average	61.26	17.89	2.315
Standard Deviation	0.250	0.120	0.019
RSD	0.406	0.685	0.838

The balls and jar are usually worn during MA due to the mechanical impactions. Therefore, contamination will be introduced into the materials. Although zirconia balls (diameters: 3 mm and 5 mm, mixed with a mass ratio of 1:1) and zirconia ball milling jars (volume: 50 cm^3, wrapped in stainless steel shell) is one of the most wear-resistant options for MA. In addition, zirconia is proved to be inert for hydrogen evolution reaction.[2]

References

1 R. S. Kalubarme, A. I. Inamdar, D. S. Bhange, H. Im, S. W. Gosavi and C. J. Park, *J. Mater. Chem. A*, 2016, **4**, 17419–17430.

2 H. Tao, C. Choi, L. X. Ding, Z. Jiang, Z. Han, M. Jia, Q. Fan, Y. Gao, H. Wang, A. W. Robertson, S. Hong, Y. Jung, S. Liu and Z. Sun, *Chem*, 2019, **5**, 204–214.

3 T. Acharya and Choudhary, *J. Electron. Mater.*, 2015, **44**, 271–280.

4 E. Gileadi, *Electrode kinetics for chemists, chemical engineers, and materials scientists*, VCH, 1993.

5 J. P. Perdew, K. Burke and M. Ernzerhof, *Phys. Rev. Lett.*, 1996, **77**, 3865–3868.

6 G. Kresse and J. Furthmüller, *Comput. Mater. Sci.*, 1996, **6**, 15–50.

7 G. Kresse, *J. Non. Cryst. Solids*, 1995, **192–193**, 222–229.

8 G. Kresse and J. Hafner, *Phys. Rev. B*, 1994, **49**, 14251–14269.

9 P. E. Blöchl, *Phys. Rev. B*, 1994, **50**, 17953.

10 D. Joubert, *Phys. Rev. B - Condens. Matter Mater. Phys.*, 1999, **59**, 1758–1775.

11 J. D. Pack and H. J. Monkhorst, *Phys. Rev. B*, 1977, **16**, 1748–1749.

12 G. Henkelman, B. P. Uberuaga and H. Jónsson, *J. Chem. Phys.*, 2000, **113**, 9901–9904.

13 V. Viswanathan, H. A. Hansen, J. Rossmeisl and J. K. Nørskov, *ACS Catal.*, 2012, **2**, 1654–1660.

14 J. K. Nørskov, J. Rossmeisl, A. Logadottir, L. Lindqvist, J. R. Kitchin, T. Bligaard and H. Jónsson, *J. Phys. Chem. B*, 2004, **108**, 17886–17892.

15 L. I. Bendavid and E. A. Carter, *J. Phys. Chem. C*, 2013, **117**, 26048–26059.

16 N. A. Merino, B. P. Barbero, P. Eloy and L. E. Cadús, *Appl. Surf. Sci.*, 2006, **253**, 1489–1493.

17 M. You, T. G. Kim and Y. M. Sung, *Cryst. Growth Des.*, 2010, **10**, 983–987.

18 J. Intrater, *Mater. Manuf. Process.*, 2007, **22**, 790–791.

19 C. Suryanarayana, *J. Alloys Compd.*, 2011, **509**, S229–S234.

20 J. C. McGlynn, T. Dankwort, L. Kienle, N. A. G. Bandeira, J. P. Fraser, E. K. Gibson, I. Cascallana-Matías, K. Kamarás, M. D. Symes, H. N. Miras and A. Y. Ganin, *Nat. Commun.*, 2019, **10**, 1–9.

21 B. Lu, L. Guo, F. Wu, Y. Peng, J. E. Lu, T. J. Smart, N. Wang, Y. Z. Finfrock, D. Morris, P. Zhang, N. Li, P. Gao, Y. Ping and S. Chen, *Nat. Commun.*, 2019, **10**, 631.

22 Y. Xie, J. Cai, Y. Wu, Y. Zang, X. Zheng, J. Ye, P. Cui, S. Niu, Y. Liu, J. Zhu, X. Liu, G. Wang and Y. Qian, *Adv. Mater.*, 2019, **31**, 1807780.

23 F. Yu, H. Zhou, Y. Huang, J. Sun, F. Qin, J. Bao, W. A. Goddard, S. Chen and Z. Ren, *Nat. Commun.*, 2018, **9**, 2551.

24 J. Zhang, T. Wang, P. Liu, Z. Liao, S. Liu, X. Zhuang, M. Chen, E. Zschech and X. Feng, *Nat. Commun.*, 2017, **8**, 15437.

25 Q. Wu, M. Luo, J. Han, W. Peng, Y. Zhao, D. Chen, M. Peng, J. Liu, F. M. F. De Groot and Y. Tan, *ACS Energy Lett.*, 2020, **5**, 192–199.

26 Z. Zhang, G. Liu, X. Cui, B. Chen, Y. Zhu, Y. Gong, F. Saleem, S. Xi, Y. Du, A. Borgna, Z. Lai, Q. Zhang, B. Li, Y. Zong, Y. Han, L. Gu and H. Zhang, *Adv. Mater.*, 2018, **30**, 1801741.

27 P. Jiang, Y. Yang, R. Shi, G. Xia, J. Chen, J. Su and Q. Chen, *J. Mater. Chem. A*, 2017, **5**, 5475–5485.

28 Y. Wu, X. Liu, D. Han, X. Song, L. Shi, Y. Song, S. Niu, Y. Xie, J. Cai, S. Wu, J. Kang, J. Zhou, Z. Chen, X. Zheng, X. Xiao and G. Wang, *Nat. Commun.*, 2018, **9**, 1425.

29 Y. Zang, S. Niu, Y. Wu, X. Zheng, J. Cai, J. Ye, Y. Xie, Y. Liu, J. Zhou, J. Zhu, X. Liu, G. Wang and Y. Qian, *Nat. Commun.*, 2019, **10**, 1217.

30 C. Lu, D. Tranca, J. Zhang, F. RodrÍguez Hernández, Y. Su, X. Zhuang, F. Zhang, G. Seifert and X. Feng, *ACS Nano*, 2017, **11**, 3933–3942.

31 Z. Liu, Z. Li, J. Li, J. Xiong, S. Zhou, J. Liang, W. Cai, C. Wang, Z. Yang and H. Cheng, *J. Mater. Chem. A*, 2019, **7**, 5621–5625.

32 Y. Y. Chen, Y. Zhang, W. J. Jiang, X. Zhang, Z. Dai, L. J. Wan and J. S. Hu, *ACS Nano*, 2016, **10**, 8851–8860.

33 A. B. Laursen, K. R. Patraju, M. J. Whitaker, M. Retuerto, T. Sarkar, N. Yao, K. V. Ramanujachary, M. Greenblatt and G. C. Dismukes, *Energy Environ. Sci.*, 2015, **8**, 1027–1034.

34 R. Zhang, X. Wang, S. Yu, T. Wen, X. Zhu, F. Yang, X. Sun, X. Wang and W. Hu, *Adv. Mater.*, 2017, **29**, 1605502.

35 Y. Tan, H. Wang, P. Liu, C. Cheng, F. Zhu, A. Hirata and M. Chen, *Adv. Mater.*, 2016, **28**, 2951–2955.

36 W. Zhu, C. Tang, D. Liu, J. Wang, A. M. Asiri and X. Sun, *J. Mater. Chem. A*, 2016, **4**, 7169–7173.

37 X. Peng, A. M. Qasim, W. Jin, L. Wang, L. Hu, Y. Miao, W. Li, Y. Li, Z. Liu, K. Huo, K. yin Wong and P. K. Chu, *Nano Energy*, 2018, **53**, 66–73.

38 T. Liu, P. Li, N. Yao, T. Kong, G. Cheng, S. Chen and W. Luo, *Adv. Mater.*, 2019, **31**, 1806672.

39 B. Liu, Y. F. Zhao, H. Q. Peng, Z. Y. Zhang, C. K. Sit, M. F. Yuen, T. R. Zhang, C. S. Lee and W. J. Zhang, *Adv. Mater.*, 2017, **29**, 1606521.

40 L. Cao, Q. Luo, W. Liu, Y. Lin, X. Liu, Y. Cao, W. Zhang, Y. Wu, J. Yang, T. Yao and S. Wei, *Nat. Catal.*, 2019, **2**, 134–141.

41 Y. Huang, Q. Gong, X. Song, K. Feng, K. Nie, F. Zhao, Y. Wang, M. Zeng, J. Zhong and Y. Li, *ACS Nano*, 2016, **10**, 11337–11343.

42 C. Dong, X. Liu, X. Wang, X. Yuan, Z. Xu, W. Dong, M. S. Riaz, G. Li and F. Huang, *J. Mater. Chem. A*, 2017, **5**, 24767–24774.